Chemical Science

ROYAL SOCIETY OF CHEMISTRY

EDGE ARTICLE

View Article Online
View Journal | View Issue

Cite this: *Chem. Sci.*, 2021, **12**, 13888

All publication charges for this article have been paid for by the Royal Society of Chemistry

Received 23rd July 2021
Accepted 28th September 2021

DOI: 10.1039/d1sc04045f

rsc.li/chemical-science

Development of a panchromatic photosensitizer and its application to photocatalytic CO_2 reduction†

Mari Irikura, Yusuke Tamaki* and Osamu Ishitani *

We designed and synthesized a heteroleptic osmium(II) complex with two different tridentate ligands, **Os**. **Os** can absorb the full wavelength range of visible light owing to S–T transitions, and this was supported by TD-DFT calculations. Excitation of **Os** using visible light of any wavelength generates the same lowest triplet metal-to-ligand charge-transfer excited state, the lifetime of which is relatively long (τ_{em} = 40 ns). Since excited **Os** could be reductively quenched by 1,3-dimethyl-2-(*o*-hydroxyphenyl)-2,3-dihydro-1*H*-benzo[*d*]imidazole, **Os** displays high potential as a panchromatic photosensitizer. Using a combination of **Os** and a ruthenium(II) catalyst, CO_2 was photocatalytically reduced to HCOOH *via* irradiation with 725 nm light, and the turnover number reached 81; irradiation with light at λ_{ex} > 770 nm also photocatalytically induced HCOOH formation. These results clearly indicate that **Os** can function as a panchromatic redox photosensitizer.

Introduction

In recent years, various photocatalytic reactions toward artificial photosynthesis for CO_2 reduction,[1,2] H_2 evolution,[3] and water oxidation[4] using metal complexes have attracted attention. Because these reactions are multi-electron processes, two functions are required: a redox photosensitizer that absorbs visible light and initiates electron transfer from its excited state and a catalyst that accepts electrons or holes and activates substrates through multi-electron processes. For effective utilization of solar light, absorption of visible light over a wide range of wavelengths by redox photosensitizers is highly important. For example, light in the 280–550 nm wavelength range covers only 14% of total solar irradiance in AM1.5G conditions, while 280–800 nm light covers 40%.[5] The use of a panchromatic redox photosensitizer that can absorb the full wavelength range of visible light is promising for increasing the utilization efficiency of solar energy.

Photoredox catalysts, another name for redox photosensitizers, also play critical roles in many photochemical organic reactions.[6] In these photocatalytic reactions, light absorption by co-existing components, such as a catalyst and/or substrate, frequently causes side reactions and the inner-filter effect, which lowers the efficiency of photocatalysis by inhibiting light absorption by the photosensitizer. For this reason, the development of redox photosensitizers that can absorb longer wavelength light is also important.

Ruthenium(II) tris-diimine complexes, $[Ru(N^N)_3]^{2+}$ (N^N = diimine ligand), are the most frequently used redox photosensitizers because they absorb visible light, owing to singlet metal-to-ligand charge-transfer (^{1}MLCT) transitions, and their lowest triplet MLCT (^{3}MLCT) excited states that are rapidly and quantitatively produced by the intersystem crossing from the ^{1}MLCT states have long lifetimes ranging from several hundred ns to several μs.[7,8] They also have appropriate redox potentials for various reactions. However, $[Ru(N^N)_3]^{2+}$ as photosensitizers have the disadvantage of limited visible light absorption, typically $[Ru(bpy)_3]^{2+}$ (bpy = 2,2′-bipyridine) can absorb only the light at λ_{abs} < 550 nm; therefore, many of the reported $[Ru(N^N)_3]^{2+}$-type redox photosensitizers cannot utilize lower-energy visible light. A simple strategy to extend the wavelength range of light absorption is to decrease the energy gap between the highest occupied molecular orbital (HOMO) and lowest unoccupied molecular orbital (LUMO); however, this usually shortens the lifetime of the excited state owing to the energy gap law and decreases the reducing/oxidizing power of the complex. For this reason, the reported ruthenium(II) complexes with panchromatic and near-infrared absorption, which are employed in dye-sensitized solar cells,[9,10] cannot be utilized as redox photosensitizers for photocatalytic reactions. One example of a ruthenium(II) photosensitizer with longer-wavelength absorption is a trinuclear ruthenium(II) complex bridged by 1,4,5,8,9,12-hexaazatriphenylene (HAT), $[\{(dmb)_2Ru\}_3(\mu\text{-HAT})]^{6+}$ (dmb = 4,4′-dimethyl-2,2′-bipyridine), which

Department of Chemistry, School of Science, Tokyo Institute of Technology, O-okayama 2-12-1-NE-1, Meguro-ku, Tokyo, 152-8550, Japan. E-mail: tamaki@chem.titech.ac.jp; ishitani@chem.titech.ac.jp

† Electronic supplementary information (ESI) available: DFT-calculated characteristics of **Os**; emission quenching experiment; Franck–Condon analysis of emission spectrum with vibronic structure of **Os**; mirror image of S–T absorption and phosphorescence of **Os**; cyclic voltammogram of BI(OH)H; quantum yield for HCOOH production; visible absorption spectra of **Os**, **Ru(CO)** and BI(OH)H. See DOI: 10.1039/d1sc04045f

has been used as a redox photosensitizer to drive H_2 evolution.[11] In this case, the ion-pair adducts of $[\{(dmb)_2Ru\}_3(\mu\text{-HAT})]^{6+}$ and ascorbate anions have been reported to afford static reductive quenching and increased reducing power, which compensated for the disadvantage of a smaller HOMO–LUMO gap. However, the reducing power of this adduct is still insufficient for driving CO_2 reduction, which requires stronger reducing power than does H_2 evolution.

Another strategy for achieving longer-wavelength absorption is to utilize the direct transition from the ground state to the triplet excited state (S–T transition). Although this is usually a spin-flip-forbidden transition, many osmium(II) complexes give S–T absorption bands owing to strong spin–orbit coupling due to the heavy atom effect of osmium. For example, $[Os(tpy)_2]^{2+}$ (tpy = 2,2′:6′,2″-terpyridine) has given an S–T absorption band at 600–750 nm and been employed as a photosensitizer for organic synthesis[12] and H_2 evolution.[13] We also previously reported that $[Os(5dmb)_2(dmb)]^{2+}$ (5dmb = 5,5′-dimethyl-2,2′-bipyridine) functions as a photosensitizer and catalyzes CO_2 reduction in combination with a rhenium(I) catalyst under red light irradiation (λ_{ex} > 620 nm).[14] However, these osmium(II) complexes do not absorb the full wavelength range of visible light up to 800 nm (Fig. 1).

Therefore, in this study, we developed a redox photosensitizer that displays panchromatic absorption. A heteroleptic osmium(II) complex with two different tridentate ligands, [(mbip)Os(mtpy)]$^{2+}$ (**Os** in Chart 1: mbip = bis(*N*-methylbenzimidazolyl)pyridine; mtpy = 4′-methyl-2,2′:6′,2″-terpyridine), was designed and synthesized. The stronger σ-donation of the methylbenzimidazole units should induce longer-wavelength absorption. Although a similar complex, [(mbip)Os(tpy)]$^{2+}$, has been reported, its photochemical and photosensitizing properties have not been investigated.[15] In this study, the photophysical, photochemical, and photosensitizing properties of **Os** were investigated, and **Os** was successfully applied to the photocatalytic reduction of CO_2 as the first panchromatic redox photosensitizer in combination with a ruthenium(II) catalyst, **Ru(CO)** (Chart 1).

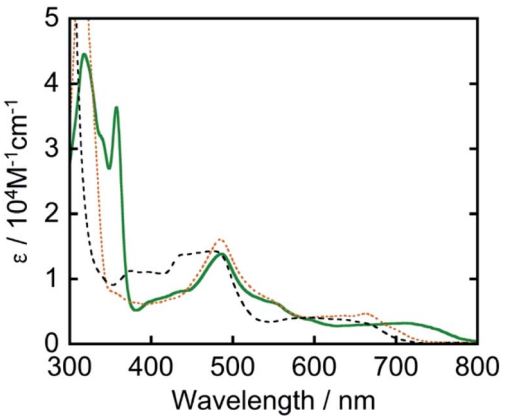

Fig. 1 UV-vis absorption spectrum of **Os** (green solid line) measured in DMA along with those of $[Os(5dmb)_2(dmb)]^{2+}$ in *N*,*N*-dimethylformamide (black broken line) and $[Os(mtpy)_2]^{2+}$ in DMA (orange dashed line).

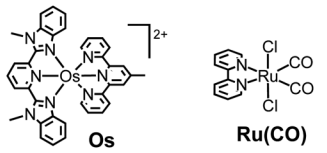

Chart 1 Structures and abbreviations of the complexes used. Counter anions were PF_6^-.

Results and discussion

The heteroleptic osmium(II) complex with two tridentate ligands was synthesized through the three steps shown in eqn (1). $[(mbip)OsCl_3]$ was dimerized into $[Os(mbip)(\mu\text{-Cl})Cl]_2$ to remove the byproduct of $[Os(mbip)_2]^{2+}$ by exploiting the insolubility of $[Os(mbip)(\mu\text{-Cl})Cl]_2$ in ethanol. The target complex, **Os**, was isolated using ion-exchange column chromatography.

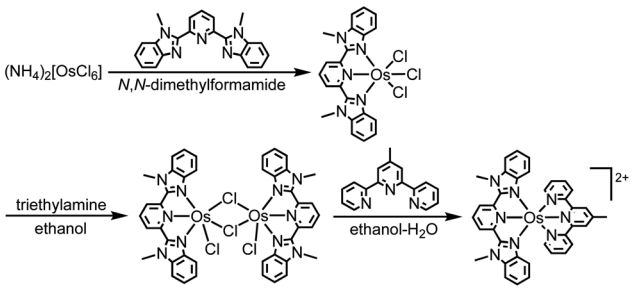

(1)

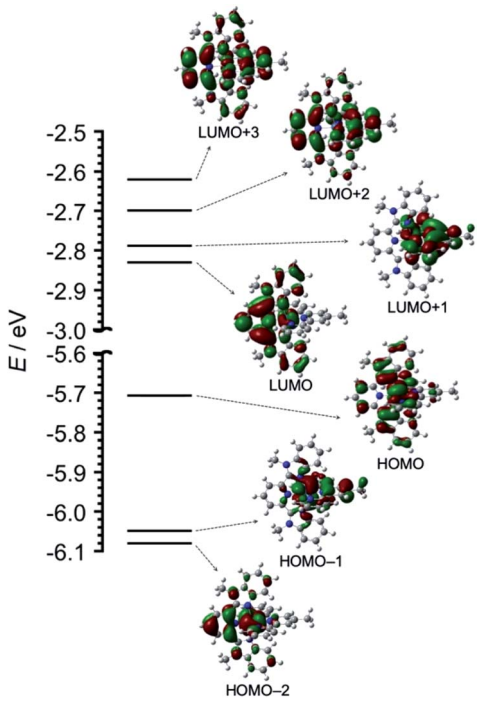

Fig. 2 DFT-calculated energy diagram and isodensity plots of frontier molecular orbitals of **Os**. The left portions of the structures are mbip. All orbitals were computed at an isovalue of 0.02.

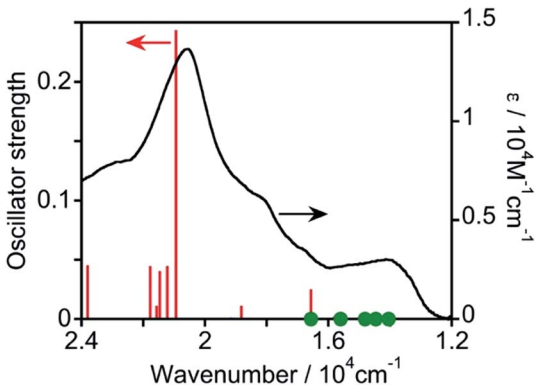

Fig. 3 Calculated oscillator strengths of S–S transitions (red lines) and UV-vis absorption spectrum of **Os** measured in DMA (black line). Green filled circles (●) indicate the calculated energies of S–T transitions.

The ultraviolet-visible (UV-vis) absorption spectrum of **Os** measured in *N*,*N*-dimethylacetamide (DMA) is shown in Fig. 1. **Os** gave longer-wavelength absorption bands at 620–800 nm (λ_{max} = 709 nm, $\varepsilon = 3.20 \times 10^3$ M^{-1} cm^{-1}) attributable to S–T transitions to ^{3}MLCT excited states as well as bands attributed to π–π* transitions of the tridentate ligands at 300–360 nm and ^{1}MLCT transitions at λ_{max} = 487 nm ($\varepsilon = 1.38 \times 10^4$ M^{-1} cm^{-1}). The S–T transition bands should be observed because of the heavy atom effect of osmium, which enhances spin–orbit coupling. The spectra of other osmium(II) complexes that have been used as photosensitizers are also shown in Fig. 1. It should be noted that only **Os** can absorb full-wavelength range of visible light with a relatively high molar absorptivity.

The geometry, molecular orbitals, and absorption spectrum of **Os** were analyzed using density functional theory/time-dependent density functional theory (DFT/TD-DFT) calculations using Gaussian 16.[16] The geometry optimization of **Os** was performed in DMA using the B3LYP exchange–correlation functional and LanL2DZ basis set for osmium and 6-311++G(d,p) for the ligands. Tridentate ligands mbip and mtpy were coordinated on osmium perpendicular to each other. Fig. 2 shows the frontier molecular orbitals of **Os**, and Table S1† summarizes their characteristics. HOMO−2, HOMO−1, and HOMO received major contributions from the osmium(II) center and minor contributions from the ligands. The energy levels of the LUMO and LUMO+1 were very close (ΔE = 0.04 eV). The LUMO and LUMO+1 received major contributions from mbip and mtpy, respectively. LUMO+2 and LUMO+3 were distributed on both mbip and mtpy.

Then, TD-DFT calculations were performed based on the geometry optimized using DFT calculations. Fig. 3 displays the calculated oscillator strengths of the excitations and the observed spectrum, and Table 1 summarizes the characteristics of the excitations. The observed ^{1}MLCT absorption band at λ_{max} = 487 nm was consistent with the singlet-to-singlet (S–S) transition at 20 940 cm^{-1} (= 478 nm, #17 in Table 1) with a high oscillator strength of 0.242. This excitation received a major contribution from the HOMO−1 → LUMO+1 transition (57%) and a partial contribution from the HOMO−2 → LUMO (24%) and HOMO → LUMO+2 (16%) transitions, indicating that the excitation is predominantly the MLCT from osmium(II) to the mtpy ligand. Because TD-DFT calculations using Gaussian 16 do not consider spin–orbit couplings, the oscillator strength of every S–T transition cannot be calculated. A spin-forbidden S–T transition gains strength by borrowing the intensity of the oscillator strength of the spin-allowed S–S transition (f_s). Considering the coupling of S–T transitions with S–S transitions, effective coupling should occur only between S–T and S–S transitions involving different d orbitals and common π* orbitals.[17–20] As shown in Table 1, therefore, the S–T transitions of #1 and #3 couple with the S–S transition of #17, which has high oscillator strength (f_s = 0.242), although the energy gaps are relatively large ($\Delta E_{S-T} = 6–7 \times 10^3$ cm^{-1}). The S–T transitions of #2 and #4 strongly couple with the S–S transition of #6, which has low oscillator strength (f_s = 0.024) because of the smaller energy gap ($\Delta E_{S-T} = 1–2 \times 10^3$ cm^{-1}). The S–T transition of #7 can couple weakly with the S–S transitions of #18 (f_s = 0.044), #21 (f_s = 0.039), and #23 (f_s = 0.044). Thus, the S–T transitions of #1 to #4 should gain oscillator strength by

Table 1 Excitation characteristics of **Os**[a]

#	Energy/cm^{-1}	Oscillator strength	Multiplicity	Major transitions		
1	14 054		Triplet	H → L (98%)		
2	14 470			H−2 → L (82%)	H−1 → L+1 (15%)	
3	14 819			H → L+1 (96%)		
4	15 613			H−2 → L (15%)	H−1 → L+1 (79%)	
7	16 579			H → L+2 (30%)	H → L+3 (60%)	
6	16 564	0.024	Singlet	H → L+1 (98%)		
12	18 820	0.010		H−1 → L+1 (11%)	H → L+2 (81%)	
17	20 940	0.242		H−2 → L (24%)	H−1 → L+1 (57%)	H → L+2 (16%)
18	21 219	0.044		H−1 → L+2 (92%)		
21	21 466	0.039		H−2 → L+2 (99%)		
23	21 778	0.044		H−2 → L+3 (98%)		

[a] Calculated using TD-DFT at the B3LYP/LanL2DZ (Os)/6-311++G(d,p) level of theory. The HOMO and LUMO are represented by H and L, respectively.

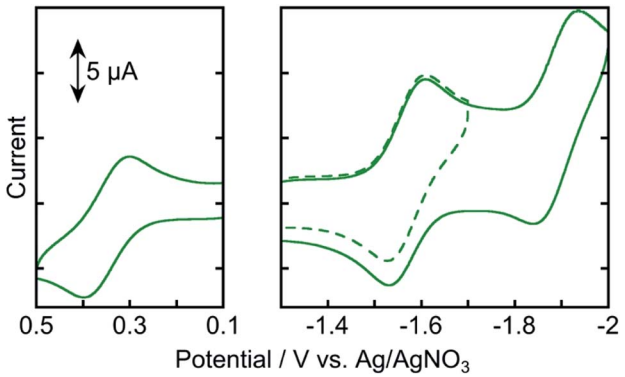

Fig. 4 Cyclic voltammograms of **Os** (0.5 mM) in an Ar-saturated DMA solution containing Et_4NBF_4 (0.1 M) as a supporting electrolyte with a $Ag/AgNO_3$ (10 mM) reference electrode. Scan rate was 0.2 V s^{-1}.

coupling with spin-allowed S–S transitions. They have lower energy than the lowest-energy S–S transition (#6) and their energy is consistent with the observed absorption band in the lower-energy region (1.3–1.6 × 10^4 cm^{-1}). Therefore, these S–T transitions should contribute to absorption in the longer-wavelength region.

Fig. 4 shows the cyclic voltammogram of **Os** measured in an Ar-saturated DMA solution. Three reversible redox couples were observed at +0.35, −1.57, and −1.89 V *vs.* $Ag/AgNO_3$. The oxidation wave at $E^{ox}_{1/2}$ = +0.35 V was attributed to the one-electron oxidation of osmium(II), and the reduction waves at $E^{red}_{1/2}$ = −1.57 and −1.89 V were attributed to the subsequent one-electron reduction of the tridentate ligands. These results indicate that the one-electron-reduced species (OERS) of **Os** has relatively strong reducing power and is stable at least on the time scale of cyclic voltammetry measurement at a scan rate of 0.2 V s^{-1}.

Os exhibited phosphorescence at λ_{max} = 795 nm in an Ar-saturated DMA solution upon excitation with visible light (λ_{ex} = 456 nm). The emission quantum yield was Φ_{em} = 0.3%. The emission lifetime was determined to be τ_{em} = 40 ns from single-exponential fitting of the transient emission (Fig. S1†). Although longer-wavelength absorption and a longer lifetime in the excited state are commonly in a trade-off relationship because of the energy gap law which gives faster non-radiative decay at smaller energy gap, **Os** displayed panchromatic absorption and a relatively long lifetime, enabling initiation of the electron transfer process. These results indicate that **Os** has essential photophysical properties as a redox photosensitizer. Fig. 5 displays the emission spectra following excitation with visible light at three different wavelengths and the excitation spectrum derived from emission intensity. The emission spectra of **Os** following the excitation of the ^{1}MLCT or ^{3}MLCT absorption band at λ_{ex} = 450, 550, and 700 nm had very similar shapes (Fig. 5a). The shape of the excitation spectrum derived from the emission intensity at λ_{max} = 795 nm is quite similar to that of the absorption spectrum of **Os** (Fig. 5b). These results clearly indicate that both the ^{1}MLCT and ^{3}MLCT excited states of **Os** relax to the same lowest ^{3}MLCT excited state very rapidly, and this excited state deactivates to the ground state through radiative and non-radiative decay processes. Therefore, visible-light irradiation of **Os** at any wavelength generates the same lowest ^{3}MLCT excited state with τ_{em} = 40 ns.

Fig. S2† shows the emission spectra of **Os** in CO_2-saturated DMA solutions containing 1,3-dimethyl-2-(*o*-hydroxyphenyl)-2,3-dihydro-1*H*-benzo[*d*]imidazole (BI(OH)H) at five different concentrations. The emission intensities decreased at higher BI(OH)H concentrations, indicating that BI(OH)H quenches the excited state of **Os** (Fig. S2a†). By using Stern–Volmer plots of the emission quenching (Fig. S2b†) and the lifetime of the emission (τ_{em} = 40 ns), the quenching rate constant was determined to be k_q = 1.8 × 10^8 M^{-1} s^{-1}. The quenching fraction of excited **Os** due to BI(OH)H (0.2 M) was η_q = 60% according to the equation $\eta_q = k_q\tau_{em}[BI(OH)H]/(1 + k_q\tau_{em}[BI(OH)H])$; the reaction conditions were the same as those for photocatalytic CO_2 reduction described below. To determine the product after excited **Os** was quenched by BI(OH)H, the absorption spectral changes during photoirradiation were measured.

The absorption spectra of a CO_2-saturated DMA solution containing only **Os** (0.1 mM) and BI(OH)H (0.2 M), without a catalyst, during irradiation and the difference spectra from the post- and pre-irradiation spectra are shown in Fig. 6a and b, respectively. Fig. 6b clearly shows that new broad absorption bands appeared at λ_{max} = 530 and 800 nm and increased during

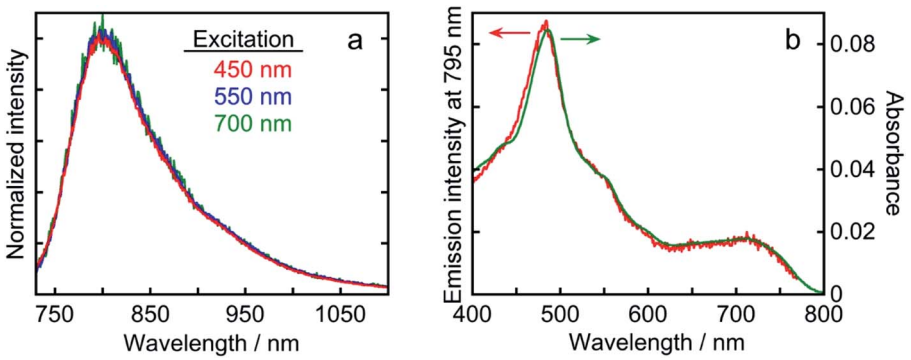

Fig. 5 (a) Emission spectra of **Os** in Ar-saturated DMA with excitation wavelengths of 450, 550, and 700 nm. (b) Excitation spectrum derived from emission intensity at λ_{max} = 795 nm in DMA (red line) and absorption spectrum of **Os** (green line).

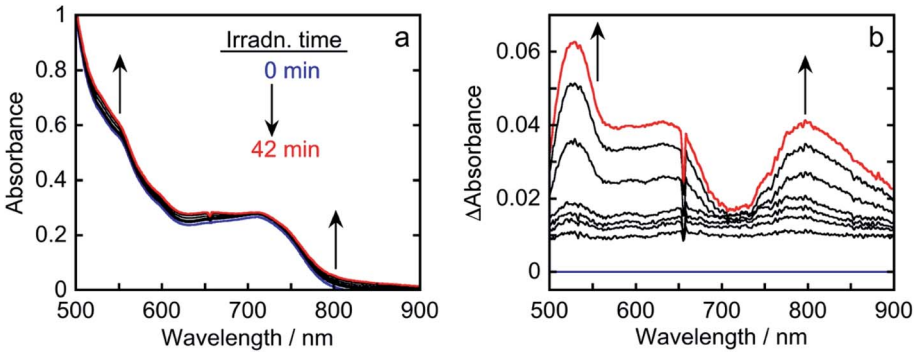

Fig. 6 (a) Absorption spectral changes of a CO_2-saturated DMA solution containing **Os** (0.1 mM) and BI(OH)H (0.2 M) during irradiation at 480 nm with a light intensity of 2.6×10^{-8} einstein s^{-1} (0–42 min at 6 min intervals) and (b) difference spectra from post- and pre-irradiation spectra. The blue and red lines represent the spectra before irradiation and after irradiation for 42 min, respectively.

irradiation. The shapes of the difference spectra were fairly similar to that of the OERS of **Os** ($\mathbf{Os}^{\bullet-}$) obtained through electro-spectroscopy using an optically transparent thin-layer electrochemical (OTTLE) cell (Fig. 7). The absorption bands due to photoirradiation disappeared after aeration of the solution, which also supports the formation of $\mathbf{Os}^{\bullet-}$, because this reduced species should be oxidized by O_2. These results clearly indicate that the ^{3}MLCT excited state of **Os** was reductively quenched by BI(OH)H to give $\mathbf{Os}^{\bullet-}$ (eqn (2)).

$$\mathbf{Os} \xrightarrow{h\nu} {}^*\mathbf{Os} \xrightarrow{\text{BI(OH)H}} \mathbf{Os}^{\bullet-} \quad (2)$$

This reductive quenching process was also supported by thermodynamics. The 0-0 transition energy of **Os** was determined to be $E_{00} = 1.59$ eV from the Franck–Condon fitting of an emission spectrum with the vibronic structure measured in frozen DMA (Fig. S3†). It is noteworthy that this value was consistent with the $E_{00} = 1.6$ eV obtained from the mirror image of S–T absorption and phosphorescence (Fig. S4†). The reduction potential of **Os** in the lowest excited state was calculated to be $E(^*\mathbf{Os}/\mathbf{Os}^{\bullet-}) = E^{red}_{1/2} + E_{00} = -1.57 + 1.59 = +0.02$ V *vs.* $Ag/AgNO_3$. The oxidation potential of BI(OH)H was measured to be $E^{ox}_{1/2}(\text{BI(OH)H}^{\bullet+}/\text{BI(OH)H}) = -0.09$ V from the cyclic voltammograms with a fast scan rate of 200 V s^{-1} using a micro glassy carbon working electrode (Fig. S5†). Therefore, electron transfer from BI(OH)H to the excited state of **Os** in the reductive quenching process should be exothermic. Hence, we can summarize the photochemistry of **Os** in the presence of BI(OH)H as follows: **Os** can absorb the full wavelength range of visible light, giving the lowest ^{3}MLCT excited state, which is reduced by BI(OH)H to generate its relatively stable OERS.

The photocatalytic reduction of CO_2 was performed using **Os** as a redox photosensitizer. $Ru(bpy)(CO)_2Cl_2$ (**Ru(CO)**), which has been used frequently as a catalyst for CO_2 reduction,[21–23] was employed because its reduction potential has been reported to be $E_p = -1.51$ V *vs.* $Ag/AgNO_3$,[24] that is, electron transfer should proceed thermodynamically from $\mathbf{Os}^{\bullet-}$ ($E_{1/2}(\mathbf{Os}/\mathbf{Os}^{\bullet-}) = -1.57$ V) to **Ru(CO)**. A CO_2-saturated DMA solution containing **Os** (50 μM), **Ru(CO)** (50 μM), and BI(OH)H (0.2 M) as a sacrificial electron donor was irradiated using a 725 nm LED light source, affording HCOOH with high selectivity (Fig. 8). After irradiation for 40 h, 8.1 μmol of HCOOH was produced along with 0.3 μmol of CO and a negligible amount of H_2 (<0.01 μmol), corresponding to turnover numbers of $TON_{HCOOH} = 81$, $TON_{CO} = 3$, and $TON_{H2} < 1$. The selectivity for HCOOH was 96%. The quantum yield for HCOOH formation was determined to be

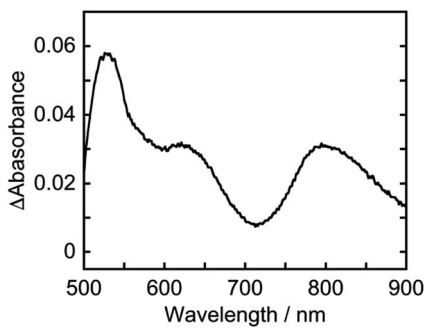

Fig. 7 Difference absorption spectrum from before and after electrolytic one-electron reduction of **Os**. A CO_2-saturated DMA solution containing **Os** (0.5 mM) and Et_4NBF_4 (0.1 M) as an electrolyte was reduced at −1.75 V using a UV-vis OTTLE cell with a Pt mesh working electrode and $Ag/AgNO_3$ reference electrode.

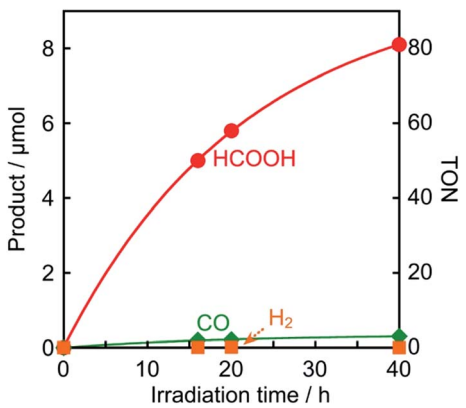

Fig. 8 Photocatalytic formation of HCOOH (●), CO (◆), and H_2 (■): CO_2-saturated DMA solutions (2 mL) containing **Os** (50 μM), **Ru(CO)** (50 μM), and BI(OH)H (0.2 M) were irradiated with 725 nm light.

Table 2 Products of photocatalysis after irradiation for 3 h[a]

Entry	Absence	Product/μmol (TON) HCOOH	CO	H_2
1	—	1.9 (19)	0.05	n.d.
2[b]	**Os**	0.04	n.d.	n.d.
3[b]	**Ru(CO)**	n.d.	n.d.	n.d.
4[b]	BI(OH)H	n.d.	n.d.	n.d.
5[c]	Light irradiation	n.d.	n.d.	n.d.
6[d]	CO_2	n.d.	n.d.	n.d.

[a] A CO_2-saturated DMA solution (2 mL) containing **Os** (50 μM), **Ru(CO)** (50 μM), and BI(OH)H (0.2 M) was irradiated with 725 nm light. [b] Photocatalytic reactions were performed without **Os**, **Ru(CO)**, or BI(OH)H. [c] The solution was placed in the dark for 3 h. [d] An Ar-saturated solution was used.

$\Phi_{HCOOH} = 0.061\%$ (Fig. S6†). Since the quenching fraction was $\eta_q = 60\%$ when [BI(OH)H] = 0.2 M, the efficiency of HCOOH formation after the reductive quenching was $\Phi_{HCOOH}/\eta_q = 0.1\%$. Table 2 summarizes the results of control experiments without **Os**, **Ru(CO)**, BI(OH)H, light irradiation, or CO_2. Entry 1 shows the result for the system with all components; that is, **Os**, **Ru(CO)**, and BI(OH)H with irradiation for 3 h under CO_2 gave $TON_{HCOOH} = 19$. Irradiation of solutions without **Os** (entry 2), **Ru(CO)** (entry 3), or BI(OH)H (entry 4) did not lead to even a catalytic amount of the products. Control experiments in the dark (entry 5) or using an Ar-saturated solution (entry 6) yielded no photocatalysis products. Because only **Os** absorbs irradiated light at 725 nm under the photocatalytic reaction conditions (Fig. S7†), these results indicate that **Os** functioned as a redox photosensitizer and drove the photocatalytic formation of HCOOH.

To determine the source of the carbon atom in the produced HCOOH, isotope labeling experiments were performed using $^{13}CO_2$. Fig. 9a and b show the $^{13}C\{^1H\}$ NMR spectra of a DMF-d_7 solution containing **Os** (0.5 mM), **Ru(CO)** (50 μM), and BI(OH)H (0.2 M) under a $^{13}CO_2$ (447 mmHg) atmosphere before and after irradiation at 725 nm using an LED for 60 h, respectively. After irradiation, a new signal appeared at 166.7 ppm, which was attributed to an equilibrium mixture of $H^{13}COOH$ and $H^{13}COO^-$ (Fig. 9b). A doublet ($^1J_{CH} = 183$ Hz) signal at 8.71 ppm in the ^1H NMR spectrum of the same solution (Fig. 10) was attributed to the methine proton of the equilibrium mixture of $H^{13}COOH$ and $H^{13}COO^-$. The absence of a clear singlet signal at 8.71 ppm attributable to the methine proton of an equilibrium mixture of $H^{12}COOH$ and $H^{12}COO^-$ indicates that HCOOH was produced through the reduction of CO_2. An identical J value of 183 Hz from the ^{13}C–^1H coupling observed in the ^{13}C NMR spectrum without ^1H decoupling (Fig. 9c) also supports the formation of $H^{13}COOH$. Therefore, we can conclude that CO_2 can be photocatalytically reduced to HCOOH using a system consisting of **Os** as the photosensitizer, **Ru(CO)** as the catalyst, and BI(OH)H as the reductant.

It is noteworthy that this system provides the first example of photocatalytic CO_2 reduction driven by only light at $\lambda_{ex} > 700$ nm. We investigated the possibility of using even longer wavelengths. Irradiation with light only at $\lambda_{ex} > 770$ nm using a xenon lamp with a short-cut filter (LI0780, Asahi Spectra Co.) to a CO_2-saturated DMA solution (4 mL) of **Os** (0.6 mM), **Ru(CO)** (50 μM), and BI(OH)H (0.2 M) for 5.5 h also gave 4.5 μmol of HCOOH, although those using $[Os(5dmb)_2(dmb)]^{2+}$ or

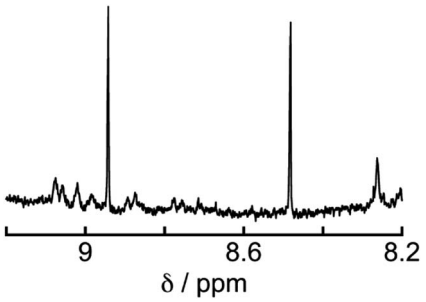

Fig. 10 ^1H NMR spectrum of the solution in Fig. 9 after irradiation.

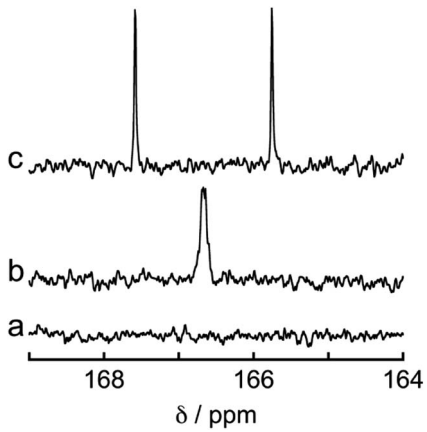

Fig. 9 $^{13}C\{^1H\}$ NMR spectra of a DMF-d_7 solution of **Os** (0.5 mM), **Ru(CO)** (50 μM), and BI(OH)H (0.2 M) under a $^{13}CO_2$ (447 mmHg) atmosphere (a) before and (b) after 60 h of irradiation. (c) ^{13}C NMR spectrum without ^1H decoupling of the same solution after irradiation.

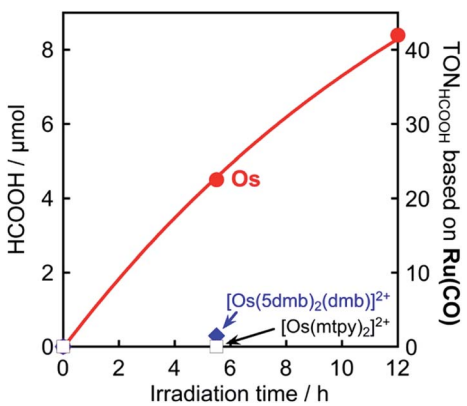

Fig. 11 Photocatalytic formation of HCOOH using light at $\lambda_{ex} > 770$ nm and **Os** (●), $[Os(5dmb)_2(dmb)]^{2+}$ (◆), or $[Os(mtpy)_2]^{2+}$ (□) as a redox photosensitizer: CO_2-saturated DMA solutions (4 mL) containing osmium(II) photosensitizer (0.6 mM), **Ru(CO)** (50 μM), and BI(OH)H (0.2 M) were irradiated.

Table 3 Photocatalytic formation of HCOOH using light at $\lambda_{ex} > 770$ nm[a]

Photosensitizer	Irradiation time/h	HCOOH/μmol	TON_{HCOOH}^{Os}	$TON_{HCOOH}^{Ru(CO)}$
Os	5.5	4.5	1.9	23
	12	8.4	3.5	42
$[Os(5dmb)_2(dmb)]^{2+}$	5.5	0.3	0.1	1.5
$[Os(mtpy)_2]^{2+}$	5.5	n.d.	—	—

[a] A CO_2-saturated DMA solution (4 mL) containing osmium(II) photosensitizer (0.6 mM), **Ru(CO)** (50 μM), and BI(OH)H (0.2 M) was irradiated using light at $\lambda_{ex} > 770$ nm.

$[Os(mtpy)_2]^{2+}$ instead of **Os** scarcely produced HCOOH (Fig. 11, Table 3). This should be due to the poor absorption of $[Os(5dmb)_2(dmb)]^{2+}$ and $[Os(mtpy)_2]^{2+}$ at $\lambda > 750$ nm as shown in Fig. 1. Further irradiation for 12 h in the same condition using **Os** gave 8.4 μmol of HCOOH which corresponds to $TON_{HCOOH} = 3.5$ based on **Os** used and $TON_{HCOOH} = 42$ based on **Ru(CO)** used. Therefore, **Os** can function as a panchromatic redox photosensitizer.

Experimental

General procedures

^{1}H NMR spectra were obtained in chloroform-*d* or acetonitrile-d_3 using a JEOL ECA400II (400 MHz) system to identify the synthesized ligands and complexes. The residual protons of chloroform-*d* or acetonitrile-d_3 were used as internal standards. Electrospray ionization-mass spectrometry (ESI-MS) was performed using a Shimadzu LCMS-2010A system with acetonitrile as the mobile phase. UV-vis absorption spectra were measured using a JASCO V-670 spectrophotometer. Prior to the emission measurements, the solutions were purged with Ar to remove dissolved O_2. Emission spectra and excitation spectra derived from emission intensity were measured using a HORIBA Fluorolog-3-21 spectrofluorometer equipped with an NIR-PMT R5509-43 near-infrared detector. The emission lifetime was determined using a HORIBA FluoroCube time-correlated single-photon counting system. The excitation light source was a NanoLED-460 pulse lamp (456 nm; pulse duration: 1.3 ns). The emission quantum yield was determined using a Quantaurus-QY Plus C13534-01 quantum yield analyzer (HAMAMATSU) using a xenon lamp with a band-pass filter (475 ± 25 nm) as the light source. Emission-quenching experiments were performed in CO_2-saturated solutions containing **Os** and BI(OH)H at five different concentrations. The quenching rate constant, k_q, was obtained from the slope of the Stern–Volmer plots of emission intensity against BI(OH)H concentration. The redox potentials of **Os** were measured in an Ar-saturated DMA solution containing **Os** (0.5 mM) and Et_4NBF_4 (0.1 M) as a supporting electrolyte *via* cyclic voltammetry using an ALS CHI-620Ex electrochemical analyzer with a glassy carbon working electrode (diameter: 3 mm), $Ag/AgNO_3$ (10 mM) reference electrode, and Pt counter electrode. The scan rate was 0.2 V s^{-1}. To determine the redox potential of BI(OH)H, a fast scan rate of 200 V s^{-1} was applied while using a micro glassy carbon electrode (diameter: 33 μm).

Emission spectral fitting

Franck–Condon analysis of the emission spectrum obtained in DMA frozen using liquid nitrogen was conducted to determine the 0-0 transition energy, E_{00}, according to the equation below:[25]

$$I(\tilde{\nu}) = \sum_{\substack{n_1=0 \\ n_2=0}}^{5} \left(\frac{E_{00} - n_1\tilde{\nu}_1 - n_2\tilde{\nu}_2}{E_{00}}\right)^4 \left(\frac{S_1^{n_1}}{n_1!}\right)\left(\frac{S_1^{n_2}}{n_2!}\right)$$

$$\exp\left[-4\ \log\ 2\left(\frac{\tilde{\nu} - E_{00} + n_1\tilde{\nu}_1 + n_2\tilde{\nu}_2}{\tilde{\nu}_{1/2}}\right)^2\right]$$

where $I(\nu)$ is the normalized intensity in the emission spectrum (wavenumber), S_i are the Huang–Rhys parameters of vibronic couplings reflecting the distortion in the acceptor modes, ν_i are the energies of the acceptor modes, and $\nu_{1/2}$ is the FWHM of the 0-0 vibronic component in the emission spectrum.

Photocatalysis

Photocatalytic reactions were performed in DMA solutions containing **Os** (50 μM), **Ru(CO)** (50 μM), and BI(OH)H (0.2 M). After it was purged with CO_2 for 20 min, the solution was irradiated. To determine the TON, a 2 mL solution in an 11 mL test tube was irradiated using a merry-go-round-type photoirradiation apparatus with an LED light source (725 nm), Iris-MG (CELL System Co.). The quantum yield was determined using a QYM-01 Shimadzu photoreaction quantum yield evaluation system; a 3.5 mL solution in a quartz cubic cell (11 mL; light pass length: 1 cm) was irradiated with 480 nm light from a 300 W xenon lamp equipped with a band-pass filter (480 nm; FWHM: 10 nm). The temperature of the solution during irradiation was maintained at 25 ± 0.1 °C using an IWAKI CTS-134A constant temperature system. The gaseous products of the photocatalysis, namely, CO and H_2, were analyzed using gas chromatography-thermal conductivity detector (GC-TCD) (GL Sciences GC323). HCOOH was analyzed using a capillary electrophoresis system (Agilent Technologies 7100L).

UV-vis absorption spectral changes during irradiation

A CO_2-saturated DMA solution (4 mL) containing **Os** (0.1 mM) and BI(OH)H (0.2 M) in a quartz cubic cell (light pass length: 1 cm) was irradiated at 480 nm using a xenon lamp equipped with a 480 nm band-pass filter (Asahi Spectra Co.) and a 5 cm-long water filter. During irradiation, UV-vis absorption spectral changes were measured using a Photal MCPD-9800

spectrophotometer. The temperature of the solution was maintained at 25 ± 0.1 °C using an IWAKI CTS-134A constant temperature system.

Electrochemical spectroscopy

A UV-vis OTTLE cell (light pass length: 1.0 mm) equipped with a Pt mesh working electrode, $Ag/AgNO_3$ (10 mM) reference electrode, and Pt counter electrode was employed for UV-vis electrochemical spectroscopy. UV-vis absorption spectral changes were measured using a Photal MCPD-9800 spectrometer. A CO_2-saturated DMA solution containing **Os** (0.5 mM) and Et_4NBF_4 (0.1 M) as the supporting electrolyte was electrolyzed using an ALS CHI-620Ex electrochemical analyzer.

Quantum chemical calculation

The calculations were performed using the Gaussian 16 program[16] using the B3LYP exchange–correlation functional. Geometry optimization was performed in DMA using a general basis set with the Los Alamos National Laboratory effective core potential LanL2DZ basis set for osmium and 6-311++G(d,p) for the other elements. The geometry was fully optimized without symmetry constraints. Frequency calculations were performed with the same level of theory to ensure that the optimized geometry was a local minimum. The fractional contributions of various groups to each molecular orbital were calculated using GaussSum[26] based on Mulliken population analysis.

TD-DFT excited state calculations of the singlet–singlet and singlet–triplet transitions were performed in DMA using the geometry optimized by DFT calculations; the same LanL2DZ and 6-311++G(d,p) basis sets were used.

Isotope labeling experiment using $^{13}CO_2$

An isotope labeling experiment using $^{13}CO_2$ was performed in a DMF-d_7 solution containing **Os** (0.5 mM), **Ru(CO)** (50 μM), and BI(OH)H (0.2 M). The solution was deaerated using the freeze–pump–thaw method prior to the introduction of $^{13}CO_2$ (447 mmHg). $^{13}C\{^1H\}$, ^{13}C, and ^1H NMR spectra were measured using a JEOL ECA400II spectrometer (100 MHz for ^{13}C NMR and 400 MHz for ^1H NMR) before and after irradiation for 60 h using a LED (725 nm) of Iris-MG (CELL System co.) as a light source. The residual carbons and protons of DMF-d_7 were used as internal standards for these measurements.

Materials

DMA was dried over 4 Å molecular sieves, distilled under reduced pressure, and kept under Ar before use. Et_4NBF_4 was dried under vacuum at 100 °C overnight prior to use. $Ru(bpy)(CO)_2Cl_2$,[27] BI(OH)H,[28,29] bis(*N*-methylbenzimidazolyl) pyridine (mbip),[30] and 4′-methyl-2,2′:6′,2″-terpyridine (mtpy)[31] were synthesized according to methods reported in the literature.

Synthesis

$[Os(mbip)Cl_3]$. A *N*,*N*-dimethylformamide solution (13 mL) containing $(NH_4)_2[Os^{IV}Cl_6]$ (258 mg, 0.59 mmol) and bis(*N*-methylbenzimidazolyl)pyridine (205 mg, 0.61 mmol) was refluxed for 1 h. After the solution had cooled to room temperature, water was added. The resulting black precipitate was collected. Yield: 335 mg (0.53 mmol, 90%).

$[Os(mbip)(\mu\text{-}Cl)Cl]_2$. A N_2-saturated ethanol solution (35 mL) containing $[Os(mbip)Cl_3]$ (333 mg, 0.53 mmol) and triethylamine (0.9 mL) was refluxed for 2 h under a N_2 atmosphere. The black precipitate was filtered hot and washed with ethanol and diethyl ether. Yield: 157 mg (0.13 mmol, 50%).

$[(mbip)Os(mtpy)](PF_6)_2$ (Os). A mixed solution of ethanol (8.5 mL) and H_2O (8.5 mL) containing Os(mbip)(μ-Cl)Cl (160 mg, 0.13 mmol) and 4′-methyl-2,2′:6′,2″-terpyridine (66 mg, 0.27 mmol) was heated at 180 °C for 1 h using a microwave reactor, Monowave 200 (Anton Paar). After the solvent was removed, the product was purified using ion-exchange column chromatography (packing material: SP Sephadex C-25; eluent: acetonitrile–water (1 : 1 v/v) containing NH_4PF_6 (0–14 mM)). Yield: 69 mg (0.060 mmol, 24%). ^1H NMR (400 MHz, acetonitrile-d_3) δ/ppm: 8.75 (s, 2H), 8.68 (d, 2H, J = 8.2 Hz), 8.30 (d, 2H, J = 7.8 Hz), 7.71 (dd, 1H, J = 8.2, 8.2 Hz), 7.61–7.53 (m, 4H), 7.39 (dd, 2H, J = 7.8, 7.8 Hz), 7.21 (d, 2H, J = 5.5 Hz), 7.00–6.94 (m, 4H), 6.00 (d, 2H, J = 8.2 Hz), 4.52 (s, 6H), 3.36 (s, 3H). ESI-MS (acetonitrile) m/z: 388 ($[M - 2PF_6^-]^{2+}$), 923 ($[M - PF_6^-]^+$). Anal. Calcd for $C_{37}H_{30}F_{12}N_8OsP_2 \cdot H_2O$: C, 40.96; H, 2.97; N, 10.33. Found: C, 40.83; H, 3.03; N, 10.39.

Conclusion

Os absorbed the entire wavelength range of visible light up to 800 nm, generating the same triplet lowest excited state. The lifetime of the resulting excited state was τ_{em} = 40 ns, which is relatively long and enabled the initiation of electron-transfer processes. Owing to longer-wavelength absorption by S–T transitions, **Os** exhibited both panchromatic absorption and a relatively long lifetime in the excited state. Excited **Os** was reductively quenched by BI(OH)H with a rate constant of $k_q = 1.8 \times 10^8\ M^{-1}\ s^{-1}$, giving an OERS with a reducing power of $E_{1/2}(Os^{\bullet -}) = -1.57$ V *vs.* $Ag/AgNO_3$. In combination with **Ru(CO)** as a catalyst, **Os** functioned as a redox photosensitizer and drove the photocatalytic reduction of CO_2 to HCOOH under light irradiation at λ_{ex} = 725 nm. This is the first example of photocatalytic CO_2 reduction *via* irradiation with λ_{ex} > 700 nm light.

Author contributions

YT and OI designed the study. MI and YT performed all experiments. YT and OI wrote the manuscript.

Conflicts of interest

There are no conflicts to declare.

Acknowledgements

The work was supported by JSPS KAKENHI Grant Number JP18H05355 and JP17H06440 in Scientific Research on

Innovative Areas "Innovations for Light-Energy Conversion (I4LEC)", and JP18K14238.

References

1 H. Takeda, C. Cometto, O. Ishitani and M. Robert, *ACS Catal.*, 2017, **7**, 70–88.
2 Y. Tamaki and O. Ishitani, *ACS Catal.*, 2017, **7**, 3394–3409.
3 H. Ozawa and K. Sakai, *Chem. Commun.*, 2011, **47**, 2227–2242.
4 S. Fukuzumi, J. Jung, Y. Yamada, T. Kojima and W. Nam, *Chem.–Asian J.*, 2016, **11**, 1138–1150.
5 G. P. Smestad, F. C. Krebs, C. M. Lampert, C. G. Granqvist, K. L. Chopra, X. Mathew and H. Takakura, *Sol. Energy Mater. Sol. Cells*, 2008, **92**, 371–373.
6 C. K. Prier, D. A. Rankic and D. W. C. MacMillan, *Chem. Rev.*, 2013, **113**, 5322–5363.
7 D. W. Thompson, A. Ito and T. J. Meyer, *Pure Appl. Chem.*, 2013, **85**, 1257–1305.
8 A. Juris, V. Balzani, F. Barigelletti, S. Campagna, P. Belser and A. von Zelewsky, *Coord. Chem. Rev.*, 1988, **84**, 85–277.
9 A. Hagfeldt, G. Boschloo, L. Sun, L. Kloo and H. Pettersson, *Chem. Rev.*, 2010, **110**, 6595–6663.
10 F. Bella, C. Gerbaldi, C. Barolo and M. Grätzel, *Chem. Soc. Rev.*, 2015, **44**, 3431–3473.
11 Y. Tsuji, K. Yamamoto, K. Yamauchi and K. Sakai, *Angew. Chem., Int. Ed.*, 2018, **57**, 208–212.
12 B. D. Ravetz, N. E. S. Tay, C. L. Joe, M. Sezen-Edmonds, M. A. Schmidt, Y. Tan, J. M. Janey, M. D. Eastgate and T. Rovis, *ACS Cent. Sci.*, 2020, **6**, 2053–2059.
13 Y. Miyake, K. Nakajima, K. Sasaki, R. Saito, H. Nakanishi and Y. Nishibayashi, *Organometallics*, 2009, **28**, 5240–5243.
14 Y. Tamaki, K. Koike, T. Morimoto, Y. Yamazaki and O. Ishitani, *Inorg. Chem.*, 2013, **52**, 11902–11909.
15 J.-Y. Shao and Y.-W. Zhong, *Inorg. Chem.*, 2013, **52**, 6464–6472.
16 M. J. Frisch, G. W. Trucks, H. B. Schlegel, G. E. Scuseria, M. A. Robb, J. R. Cheeseman, G. Scalmani, V. Barone, G. A. Petersson, H. Nakatsuji, X. Li, M. Caricato, A. V. Marenich, J. Bloino, B. G. Janesko, R. Gomperts, B. Mennucci, H. P. Hratchian, J. V. Ortiz, A. F. Izmaylov, J. L. Sonnenberg, D. Williams-Young, F. Ding, F. Lipparini, F. Egidi, J. Goings, B. Peng, A. Petrone, T. Henderson, D. Ranasinghe, V. G. Zakrzewski, J. Gao, N. Rega, G. Zheng, W. Liang, M. Hada, M. Ehara, K. Toyota, R. Fukuda, J. Hasegawa, M. Ishida, T. Nakajima, Y. Honda, O. Kitao, H. Nakai, T. Vreven, K. Throssell, J. A. Montgomery, Jr., J. E. Peralta, F. Ogliaro, M. J. Bearpark, J. J. Heyd, E. N. Brothers, K. N. Kudin, V. N. Staroverov, T. A. Keith, R. Kobayashi, J. Normand, K. Raghavachari, A. P. Rendell, J. C. Burant, S. S. Iyengar, J. Tomasi, M. Cossi, J. M. Millam, M. Klene, C. Adamo, R. Cammi, J. W. Ochterski, R. L. Martin, K. Morokuma, O. Farkas, J. B. Foresman, and D. J. Fox, *Gaussian 16, Revision A.03*, Gaussian, Inc., Wallingford CT, 2016.
17 Z. Abedin-Siddique, Y. Yamamoto, T. Ohno and K. Nozaki, *Inorg. Chem.*, 2003, **42**, 6366–6378.
18 Z. Abedin-Siddique, T. Ohno, K. Nozaki and T. Tsubomura, *Inorg. Chem.*, 2004, **43**, 663–673.
19 K. Nozaki, *J. Chin. Chem. Soc.*, 2006, **53**, 101–112.
20 S. Obara, M. Itabashi, F. Okuda, S. Tamaki, Y. Tanabe, Y. Ishii, K. Nozaki and M. Haga, *Inorg. Chem.*, 2006, **45**, 8907–8921.
21 J.-M. Lehn and R. Ziessel, *J. Organomet. Chem.*, 1990, **382**, 157–173.
22 H. Ishida, K. Fujiki, T. Ohba, K. Ohkubo, K. Tanaka, T. Terada and T. Tanaka, *J. Chem. Soc., Dalton Trans.*, 1990, 2155–2160.
23 Y. Kuramochi, O. Ishitani and H. Ishida, *Coord. Chem. Rev.*, 2018, **373**, 333–356.
24 Y. Kuramochi, J. Itabashi, K. Fukaya, A. Enomoto, M. Yoshida and H. Ishida, *Chem. Sci.*, 2015, **6**, 3063–3074.
25 G. H. Allen, R. P. White, D. P. Rillema and T. J. Meyer, *J. Am. Chem. Soc.*, 1984, **106**, 2613–2620.
26 N. M. O'boyle, A. L. Tenderholt and K. M. Langner, *J. Comput. Chem.*, 2008, **29**, 839–845.
27 P. A. Anderson, G. B. Deacon, K. H. Haarmann, F. R. Keene, T. J. Meyer, D. A. Reitsma, B. W. Skelton, G. F. Strouse, N. C. Thomas, J. A. Treadway and A. H. White, *Inorg. Chem.*, 1995, **34**, 6145–6157.
28 E. Hasegawa, T. Seida, N. Chiba, T. Takahashi and H. Ikeda, *J. Org. Chem.*, 2005, **70**, 9632–9635.
29 X.-Q. Zhu, M.-T. Zhang, A. Yu, C.-H. Wang and J.-P. Cheng, *J. Am. Chem. Soc.*, 2008, **130**, 2501–2516.
30 J. J. Concepcion, J. W. Jurss, M. R. Norris, Z. Chen, J. L. Templeton and T. J. Meyer, *Inorg. Chem.*, 2010, **49**, 1277–1279.
31 Y. Tamaki and O. Ishitani, *Faraday Discuss.*, 2017, **198**, 319–335.